

Detector diode circuit noise measurement and power supply method selection for the fiber optic seismograph

S. Niespodziany ^{a*}, A. T. Kurzych ^b, M. Dudek ^b

^a Institute of Heat Engineering, Warsaw University of Technology, 21/25 Nowowiejska St., Warsaw 00-665, Poland

^b Institute of Technical Physics, Military University of Technology, 2 gen. S. Kaliskiego St., Warsaw 00-908, Poland

Article info

Article history:

Received 14 Jun. 2020

Received in revised form 20 Jun. 2020

Accepted 20 Jun. 2020

Keywords:

fiber optic sensor, fibre optic rotational seismograph, closed loop, detector diode, avalanche photodiode, noise, spectral density.

Abstract

This paper investigates the noise levels present at various points in the FOSREM type fiber optic seismograph. The main aim of this research was to discover magnitudes of noise, introduced by various components of the analog and optical circuits of the device. First, the noise present in the electronic circuit without any optics connected is measured. Further experiments show noise levels including the detector diode not illuminated and illuminated. Additional tests were carried out to prove the necessity of analog circuitry shielding. All measurements were repeated using three powering scenarios which investigated the influence of power supply selection on noise. The results show that the electronic components provide a sufficient margin for the use of an even more precise detector diode. The total noise density of the whole device is lower than $4 \cdot 10^{-7}$ rad/(s $\sqrt{\text{Hz}}$). The use of a dedicated Insulating Power Converter as a power supply shows possible advantages, but further experiments should be conducted to provide explicit thermic confirmation of these gains.

1. Introduction

Nowadays, fiber optic sensors are high precision devices allowing measurement of various physical phenomena using light properties such as intensity, phase, polarization, or wavelength [1,2]. Such sensors can be constructed in an interferometer configuration, e.g., Fabry-Perot, Mach-Zehnder, Michelson, Sagnac or other [3,4]. They are widely used for very sensitive measurements of different physical parameters such as temperature [5], strain [6,7], pressure [8], vibration [9], rotation or torsion [10].

The topic of this paper is FOSREM – the fiber-optic system for rotational events & phenomena monitoring, an optical fiber-based rotational seismograph [11]. It detects a single-axis angular rotation of the object of interest. Due the general aspect of rotational seismology [12], the measured structure can be any civil engineering construction [13,14], or a geophysical object [15]. Its operation is based on the Sagnac effect [16,17].

Contrary to the previously investigated FOSREMs [18], a new type called FOS5 (fiber-optic seismograph 5) operates in a closed-loop mode [19] in which the phase shift of the light beam induced by rotation is further eliminated by MIOC – the multi-integrated optical circuit module. The MIOC module provides a special phase modulation scheme [20] which makes the device operate at one-point in its response characteristics [21].

Since FOS5 is designed for seismological investigation, especially for weak motion seismology applications, the maximum sensitivity as high as 10^{-8} rad/s in the period range from 10 to 100 s band is expected [22]. The appropriate design of the optical part with the use of a 10 mW light source, total optical losses of 19.63 dB and a 5000-m long single-mode fiber sensor loop wound on a diameter of 0.25 m gives a theoretical FOS sensitivity of $3.41 \cdot 10^{-8}$ rad/(s $\sqrt{\text{Hz}}$) [14]. However, the practical study of the noise characteristics of the electronic circuit used remains a critical aspect for in-field application of this device. For the above reason, this paper focuses on the analysis of the noise in the analog part of the electronic control circuit. The conducted experiments focus on the

*Corresponding author at: slawomir.niespodziany@pw.edu.pl

<https://doi.org/10.24425/opelre.2021.135830>.

1896-3757/ Association of Polish Electrical Engineers (SEP) and Polish Academic of Sciences (PAS). Published by PAS

© 2021 The Author(s). This is an open access article under the CC BY license (<http://creativecommons.org/licenses/by/4.0/>).

measurements of interferences occurring in various elements and include work with various power supply sources.

2. System architecture

The whole system [Fig. 1(a)] consists of two general parts – optical where a phase shift based on the Sagnac effect [16] is induced [Fig. 1(b)] and an electronic part which ensures an appropriate conversion of the optical phase difference into a digitally calculated rotation rate signal [Fig. 1(c)].

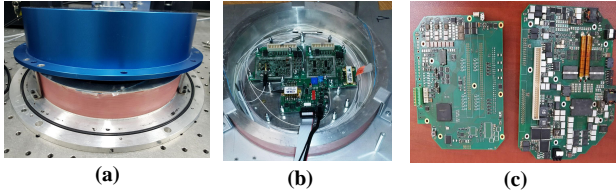


Fig. 1. General view of FOS5: (a) FOS5 with open hermetic shelling, (b) general view of the optical part with optoelectronic modules (MIOC, SLED, APD), (c) general view of the whole compact electronics.

Electronic circuit will be discussed in more detail, as it is more relevant for the cases analyzed in further sections. Nevertheless, the structure of optical circuit is also crucial to fully understand the device operation. The optical part presented in Fig. 2 is constructed according to the minimum gyro configuration which meets the system reciprocity condition [20]. SLED is the source of light travelling along the optical path (10 mW power in a single mode fiber at a 1310 nm wavelength with a spectral width of around 40 nm). The light beam travels across various optical components to reach the fiber-optical loop (5 000 m long single-mode optical fiber wound in a loop with a diameter of 0.25 m). Light beam is then split into two halves. Each half is directed to one end of the loop. It passes the loop and exits at the other end after some non-zero time (time results from the loop length). As a result of the Sagnac effect [16,17], the halves are misaligned. They are then super positioned and travel backwards in the optical path.

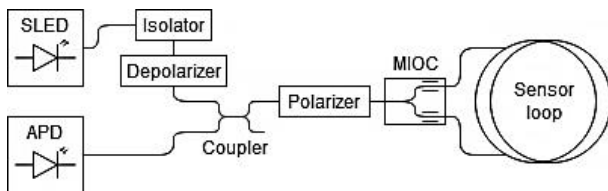


Fig. 2. Generalized optical part schema. The components interfacing electronic modules are SLED (light source), MIOC (modulating device), and APD (detector diode).

Beam misalignment is further compensated with an intentional phase shift. This phase shift is applied to the beam halves by a Modulator module (controlled by the electronic part – see Fig. 3) which drives a MIOC unit. Merging the halves, which have some, not fully compensated phase shift, reduces power of the resulting beam. This power reduction indicates the direction and magnitude of compensation that should be applied to fully eliminate the Sagnac effect. Feedback control loop uses this

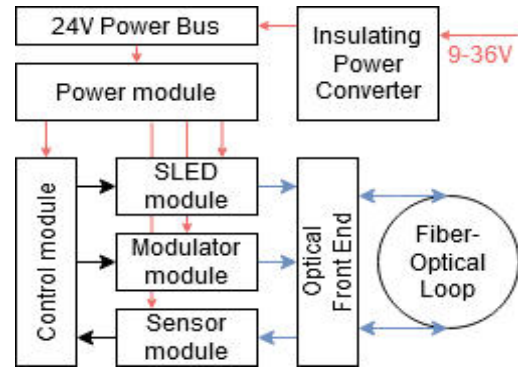


Fig. 3. General electronic part architecture. Each of SLED, Modulator, and Sensor modules handle one part of the optical circuit. They are powered by the main Power module and each has its own embedded power sub-module. Control module coordinates their operation. Power is drawn from a 24 V Power bus, which can be powered directly, or from Insulating Power Converter.

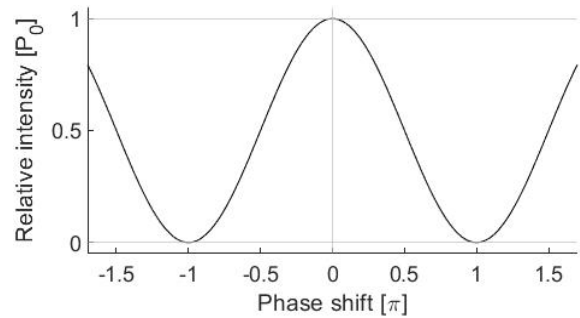


Fig. 4. Optical circuit response. Power of the returning light beam depends on the phase shift between the merged beam halves [21].

dependence to adjust the modulation scheme and determine the rotation rate. Power-to-shift dependence is shown in Fig. 4 [21]. This response function is symmetrical, and a special modulation scheme must be applied to determine the rotation direction [20].

The variable power light beam returns to the avalanche photodiode (APD in Fig. 2) where its power is measured. This is done by the sensor module (see Fig. 3). The whole process continues uninterrupted. The role of the electronic part, presented schematically in Fig. 3, is to control the operation of the SLED module (switching on and off, monitoring its temperature), drive the modulator module to apply an appropriate modulation scheme and to measure the light power using the sensor module. All these tasks must be controlled digitally. An FPGA-based control module has been used to coordinate operation of these subsystems, execute the control algorithms, and handle communications with external devices.

3. Power supply

Power requirements for each of the mentioned above modules are slightly different – each one requires few voltage levels, both positive and negative, and separate sources for the analog and digital circuitry. Each module has been provided with its own, separate, internal power unit.

It is critical to separate power supplies between the very sensitive analog modules and the high-speed digital

circuitry which could interfere with and affect the overall device performance. On the other hand, the device must be powered from a single supply. As a result of these requirements, all the modules were supplied (directly or indirectly) from the common 24 V power bus (Fig. 3). Individual power units have been designed in such way as to minimize the potential interference propagation between modules. This ensures that the crosstalk between digital and analog circuits is minimized. The 24 V Power Bus can be directly powered from an external source, but a dedicated insulating power converter (IPC) is provided on the input. Although there is a filtering stage in each power unit, the filter size and cost had to be optimized in order not to completely insulate from the outside noise. Additional filtering is required at the input of the entire powering system implemented by the input power converter.

IPC has been designed as a very low input-to-output capacitance device which presents an open circuit to any common mode interferences. Its role is not only to insulate from the outside noise, but also to adjust voltage to the range required by the internal circuitry. This allows the entire system to be powered from any voltage supply in the range of 9 V–36 V.

IPC can be omitted, by connecting the external power supply directly to the internal 24 V Power Bus, but in such case the flexibility to use the wide voltage range is no longer available and the external supply must ensure itself voltage stability and noise filtering. This is a convenient way to power the device from a stable battery source, where the voltage can be considered stable and no outside noise is present as the battery is galvanically insulated from any other circuits.

4. Research plan

The purpose of this research was to determine primarily, the noise levels in various stages of the electronic circuit, but also, secondly, to determine the effect of the power supply method on these noise levels. The main subject of the research was the sensor module, as it is the most noise sensitive part of the device.

4.1 Sensor module architecture

The sensor module consists of several stages, forming a pipeline (Fig. 5) designed to measure power of light returning from the optical circuit.

The sensing element is an avalanche photodiode (APD). The diode must be properly set up before operation. It is biased with a relatively high voltage to raise its sensitivity (bias between 40 V and 60 V). With the SLED light source turned off, the voltage is raised until a given current amount flows through a non-illuminated diode. This value is referred as “dark current”. When the desired amount of dark current flows through the diode, biasing voltage is remembered for further operations. Temperature effects should also be considered, as the diode characteristics vary during operation. The entire biasing process is controlled by the control module, as the voltage regulator (APD regulator, Fig. 5) allows digital voltage control and current measurement.

After turning SLED on, the diode will allow the working current to flow. Amount of this current is propor-

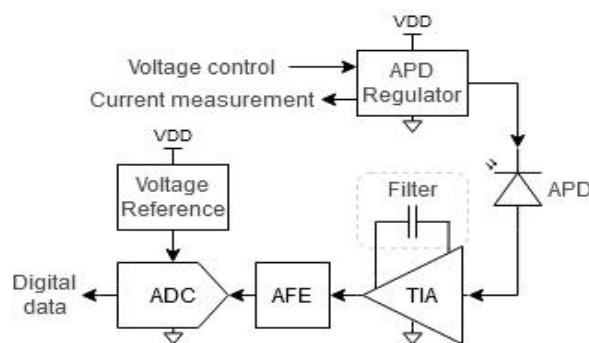


Fig. 5. Sensor module pipeline. It consists of ADC, AFE, TIA, APD, and APD Regulator.

tionally dependent on the power of the incident light. Circuit has a built-in hardware overcurrent protection mechanism which detects currents of too high values and automatically removes biasing voltage. An overcurrent alarm is signalled to the control module which can then proceed with proper actions. When biasing voltage is properly adjusted, with respect to the ambient temperature, and no overcurrent takes place, the working current flows to the trans-impedance amplifier (TIA) which converts it to voltage. TIA circuit consists of a preliminary low pass filter which cuts high frequencies outside the band of interest. The filter cut-off frequency is in the range from 500 kHz to 1000 kHz, while the signal generated and then sampled has a band of 100 kHz, so the filter impact on the signal is negligible. Preliminary filtered signal, mapped to voltage, is then adjusted in the analog front-end block (AFE) and sampled by analog to digital converter (ADC) to obtain a digital series of raw samples.

Each of these pipeline stages contribute to the overall quality of the digital signal processed further by the control module (see Fig. 3). This research investigates whether the sensor module (Fig. 3) provides enough accuracy for the optical circuit or whether there are some points where optical precision is lost at the level of electronics.

4.2 Digital pre-processing of samples

ADC residing at the end of the sensor pipeline (Fig. 5) has been used to gather all data for the research. This approach has the advantage of obtaining measurements under the same conditions as when a device operates in normal mode. In such case the measurements can be compared between each other (relative comparison), but their values have also been mapped to global units - amplitude spectral density (ASD) in $\text{rad}/(\text{s}\sqrt{\text{Hz}})$ for comparison with other systems (absolute comparison) [23].

The data presented in this paper are not raw samples obtained from ADC but have been subjected to pre-processing. This pre-processing is also carried out while a normal device operation, so the results shown reflect data that would be passed to the control algorithm.

Pre-processing is realized digitally after collecting raw samples. A resulting sample consists of several raw values ordered at the beginning and averaged after discarding several edge values (highest and lowest). The parameters for this operation are settable and both for normal operation and in case of this experiment were as follows: 4 raw samples were collected, the biggest and the smallest ones were discarded and the remaining two were averaged

resulting in one sample that was fed into the algorithm or used as experimental data.

4.3 Power supply configurations

All experiments were carried out in three configurations. Each configuration tested a different way of powering the device.

In first configuration, the device was powered with the IPC sourced from a laboratory power supply, which in turn was supplied from the mains. This was the reference measurement for the other two cases. Secondly, the laboratory power supply was replaced with an independent battery – which was assumed as a “clean” source, as it insulates the circuit from the mains. In the third case, the laboratory power supply was connected directly to the 24 V Power Bus (omitting the IPC). These three cases, further referred as “Mains + converter”, “Battery + converter” and “Mains direct” are depicted in Fig. 6. These three scenarios were applied to further measurements.

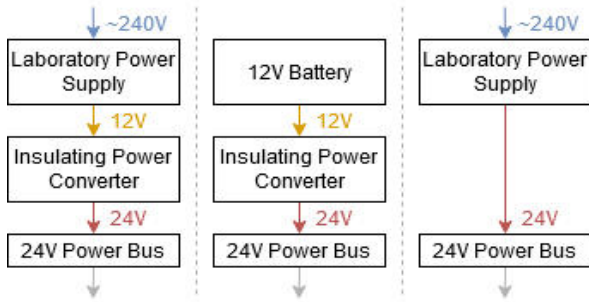


Fig. 6. Device powering schemes. Device can be powered from the mains through the IPC (left), from an insulated battery through the IPC (middle), and directly from the mains, omitting the IPC (right).

4.4 Frequency band analysis

For the electronic circuit measurements, the number of samples obtained for each experiment is over 30 000 after pre-processing (this number is limited by hardware, i.e., FPGA memory size), collected at a sampling frequency of 100 kHz. This yields a spectrum of several Hertz, up to 50 kHz. The resulting plots were calculated as the ASD noise of the measured waveforms using the Welch method [23].

Such a measuring band may appear as not fully consistent with the desired operating frequency of the device, but in fact, it is crucial for fundamental analysis of the general noise density level. Internally, the device operates at high frequency. The MIOC implementation for close-loop architecture uses the digital phase four-staircases ramp technique [19]. Its fundamental frequency is connected with sensors loop length L as $f=c/2nL$ where c is light speed and n refractive index of fiber core for operate wavelength [20]. For uses 5 000 m sensor loop this frequency is about 20.53 kHz. This signal is gained by APD regulator, and further is subjected to digital filtering, to adjust the frequency to the desired band (0.01–100 Hz). Hence a high frequency analysis is crucial for the internal device operation as well as to identify high frequency components, which could negatively impact the output (filtered) characteristics. Such interferences may be introduced for example by the switching converters present

in power supply circuit, which operate at high frequencies (see section 5).

5. Experiments

First, the noise of a stand-alone electronic circuit was analyzed (subsection 5.1 to 5.3). Then, APD was added (subsection 5.4) and further measurements were made. Finally, after enabling the SLED, data were collected to check the whole sensor module operating while connected to the optical circuit (subsection 5.5). Subsection 5.6 aggregates operation performance of the entire Sensor module.

5.1 ADC and Analog Front-End noise

Basic investigated configuration includes ADC and its Analog Front-End circuit, connected to a stable, fixed reference voltage as is shown in Fig. 7. In this configuration the noise is introduced by these electronic components and their power supply.

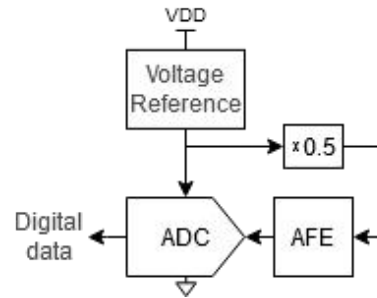


Fig. 7. ADC and Analog Front End (AFE) with reference voltage applied. The measured value is set in the middle of the measuring range. A voltage divider has been used to adjust signal level.

Figure 8 shows the ASD noise with different powering schemes applied to the given circuit.

In all three cases the mean level in a low frequency range is comparable [$3 \cdot 10^{-9}$ rad/(s $\sqrt{\text{Hz}}$)]. High spikes are introduced by the IPC in the range between 9 kHz and 15 kHz. They do not occur when powering directly from a laboratory power supply which indicates that they are a

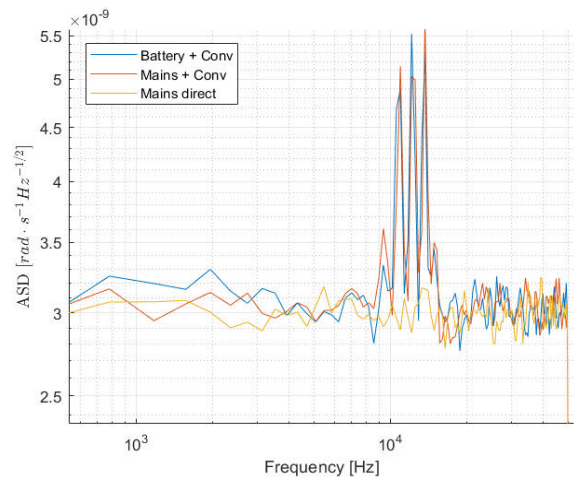


Fig. 8. ASD noise for ADC and Analog Front End Peaks are visible in the range between 9 kHz and 15 kHz, when supplying a device with IPC.

result of aliasing with one of the IPC operating frequencies: 70 kHz and 440 kHz – and the sampling frequency of 100 kHz.

5.2 Transimpedance Amplifier noise – fixed voltage

Next configuration includes the transimpedance amplifier (TIA) combined into the circuit (Fig. 9). Instead of converting current to voltage as in the target configuration, the amplifier was set to accept voltage and buffer its value. The same reference voltage was applied, as in 5.1. Except for the presence of the buffering amplifier, the circuit is identical to the previous one.

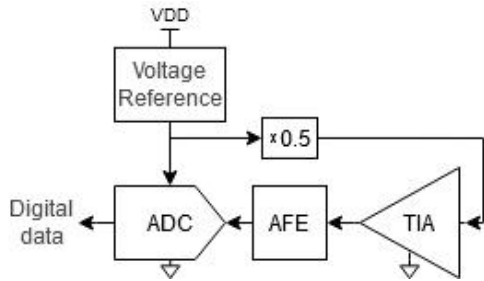


Fig. 9. Transimpedance Amplifier (TIA) in the voltage buffering configuration added.

Figure 10 shows the data obtained for this configuration. Two conclusions may be derived from it. First, peaks present in a band between 9 kHz and 15 kHz are excited by the TIA. Second, assembling the shield prevents this excitation. The average noise amplitude density (along the entire band) remains at the previously observed level. Shield assembling successfully insulates the sensitive analog circuitry from power module interferences. These results show that the separation of these circuits is of key importance, both in the sense of proper power and signal filtering, as well as physical separation and shielding.

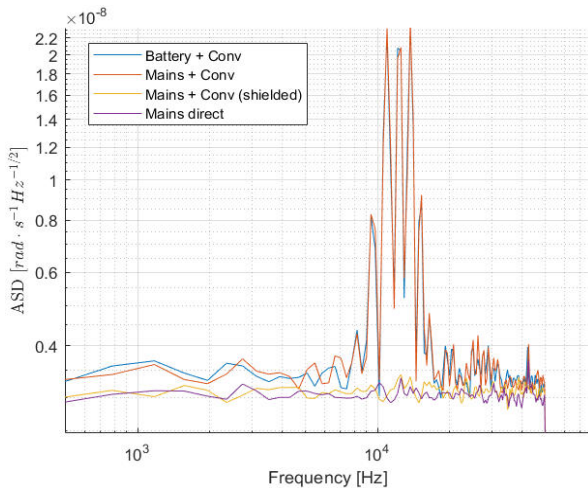


Fig. 10. ASD noise for ADC, Analog Front End and TIA. Peaks present in Fig. 8 are amplified.

5.3 Transimpedance Amplifier noise – fixed current

In the third configuration, the TIA has been set to a current-to-voltage conversion (its nominal configuration) and its input was supplied with the fixed current. Current

sourced from the APD Regulator has been adjusted and limited with a series resistor. The same regulator is also used to bias and power APD in further cases and during a normal device operation. Results of this experiment, compared to the previous ones, show the APD regulator contribution and its power supply in the noise measured. The configuration is shown in Fig. 11.

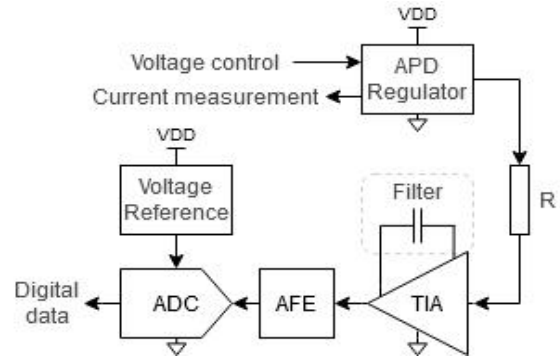


Fig. 11. TIA (with optional analog filter) supplied by a current source (current conversion configuration).

Figure 12 shows the measurement results. There is no difference when the device is powered by different supply schemes, thus, the only configuration depicted is “Mains + converter”.

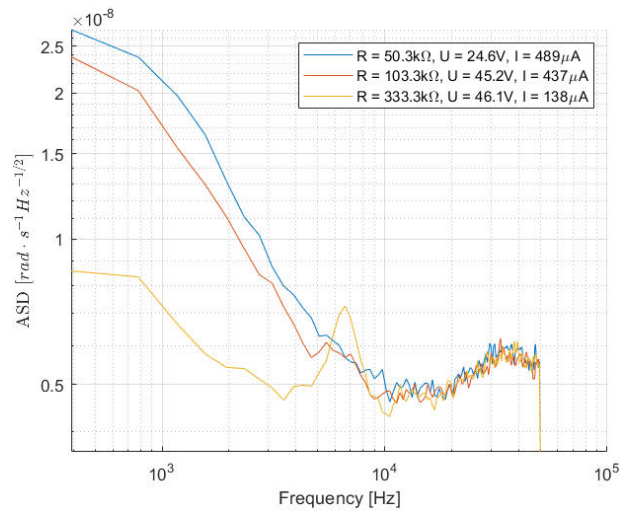


Fig. 12. ASD noise for fixed current supplied to TIA in “Mains + converter” configuration.

Compared to subsections 5.1 and 5.2, the spikes in the band between 9 kHz and 15 kHz are attenuated and no more observable. Three different operating points have been investigated for this circuit configuration. The APD regulator was set to supply lower (25 V) and higher (45 V) voltage, while, by adjusting the limiting resistor, the desired amount of current could be supplied to the TIA. The results show (by comparing plots for R = 50.3 kΩ and R = 103.3 kΩ) that the voltage level has a very limited impact on the noise level. On the other hand, lowering the current decreases the noise level in a lower frequency band (below 4 kHz). The higher attenuation effect of the increased resistance may also contribute to this tendency. The remaining peak in the range between 5 kHz and 8 kHz may be an aliasing artifact with the APD regulator power supply converter operating at the frequency of 58 kHz. It becomes visible when the regulator operates with low

current. The general range of the measured noise is consistent with previous experiments – no significant noise component is introduced by the APD regulator nor by its power supply [noise density remains in range of 10^{-8} rad/(s $\sqrt{\text{Hz}}$)].

5.4 Biased APD noise

Previous sections described solely the electronic circuit related noise – both ADC related parts and APD power supply, including different powering schemes of the entire device. Figure 13 shows the measurements of a fully assembled circuit with APD (circuit configuration shown in Fig. 5). For this measurement, the diode has not yet been illuminated by SLED. Results depict various operating points of the APD diode – biased to several dark current values, by adjusting voltage of the APD regulator. First, the effect of the analog filter and shield is tested using a low current applied (100 μA to 150 μA). Further measurements show the noise density dependence on the bias current value, with the filter and the shield. Measurements are depicted for “Mains + converter” powering scheme only, as the results do not differ between powering schemes.

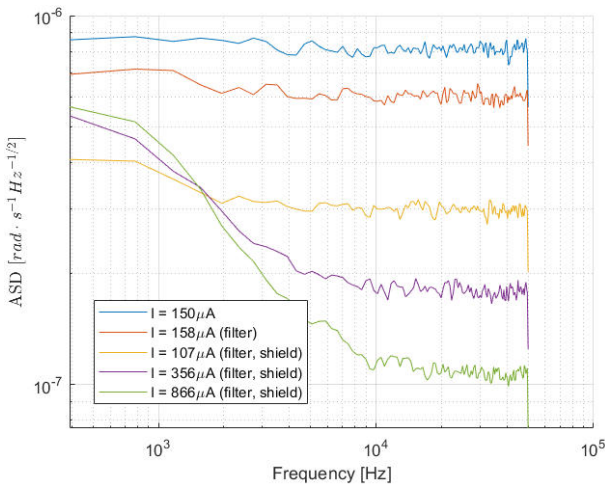


Fig. 13. Non-illuminated APD diode noise density. Higher bias current results in lowering noise density in a high frequency range.

First observation is that the measured noise magnitude rises by two orders compared to configurations without the APD diode. This noise is related to a non-illuminated APD. In general, while keeping similar current values, the analog filter and shield assembling improves the noise level. An important observation is that a further increase in the APD dark current reduces high frequency noise components, but low frequency components remain, or even get slightly amplified. This indicates that the biasing current for a normal device operation must be set to a centred value to keep a balance between reducing the mean noise level, but also to maintain its value constant over the whole band (keeping it as closest as possible to white noise).

5.5 Illuminated APD noise

The same configuration has been used to examine the illuminated APD diode. Figure 14 depicts various operating

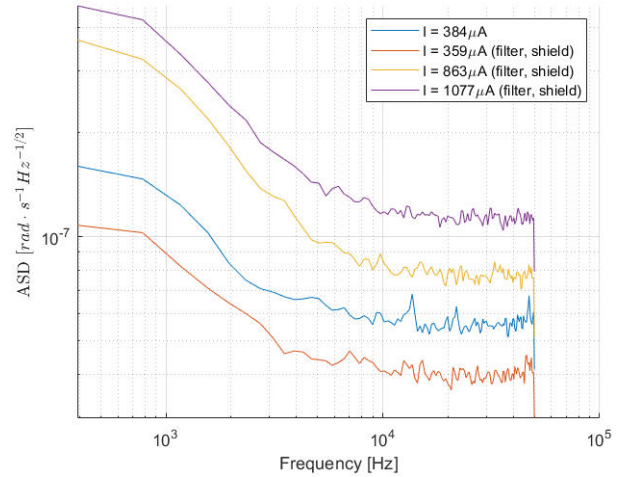


Fig. 14. Illuminated APD diode noise. A violet plot reflects nominal operating current of the APD which is set to around 1 mA in normal operation.

points of the APD after enabling SLED. Similarly to subsection 5.4, the powering scheme of the whole device did not indicate any differences in the measured noise densities, thus, only “Mains + converter” data have been plotted.

At first, a reference plot is given to compare noise between a circuit with analog filter and shield disassembled (blue) and assembled (orange). Both plots concern the same operating point of the APD. Filtering and shielding slightly decreases the general noise density level. Next, plots correspond to higher operating current values. An inverted tendency can be observed, compared to subsection 5.4, as the general noise level rises while the current being increased. This indicates different properties of the illuminated and non-illuminated APD – inverted dependence between noise and current flowing.

In such case, care must be taken to adjust the biasing voltage for a non-illuminated diode, as the noise level may increase when illuminated. Nominal operating point of the APD diode is around 1mA current which yields a noise density below $5 \cdot 10^{-7}$ rad/(s $\sqrt{\text{Hz}}$) over the band of 500 Hz to 50 kHz.

5.6 Sensor module performance

Figure 15 aggregates plots across all previous subsections. The lowest noise visible is for ADC operating solely and ADC with TIA connected, and yields $2 \cdot 10^{-9}$ rad/(s $\sqrt{\text{Hz}}$). There are power converter interferences visible but they are effectively attenuated after assembling analog filter, shield, and other circuit parts. The APD power supply introduces some additional noise which, however, resides at a relatively low level. The APD itself introduces more noise than the rest of the electronic circuit combined, but with a proper bias voltage adjustment, it can be lowered to 10^{-7} rad/(s $\sqrt{\text{Hz}}$). This level is still one order above the required, but due to the control module (FPGA) hardware limitations, low frequency (below 100 Hz) components were not examined. “APD + SLED” noise for the illuminated APD diode increases with lowering frequency and additional measurements may be conducted to investigate its full spectrum.

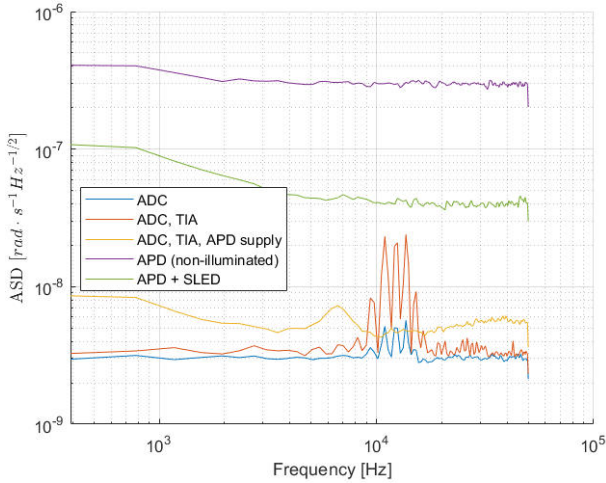


Fig. 15. ASD noise for various configurations of Sensor module. “APD + SLED” plot depicts APD in its nominal operating point (1 mA of current flowing). “Mains + converter” powering scheme was applied.

6. Powering

When testing the device in a not too noisy environment, the dependence of noise on the powering scheme is not sharp. The laboratory power supply used was a clean enough power source not to introduce any significant interferences which would be blocked by IPC and could have impact on the measured noise levels.

Most available power converters, which could be used in the application as input converters, have either a property of generating common mode interferences themselves, or these interferences are attenuated by an input-to-output capacitance added internally to the converter. In the second case, the generated interferences are at low enough level, but the input-to-output capacitance is a low impedance path for any interferences coming from the outside and this is also not acceptable.

The converter designed specifically for this application introduces visible noise peaks when examining the ADC circuit, but this noise level is much lower than levels introduced by other electronic circuit components and the APD. These noise peaks are also attenuated when the circuit is fully assembled, thus, their impact on operation is negligible. On the other side, a low input-to-output capacitance of the converter is highly beneficial if significant spikes occur on the power supply input, or a low-quality supply is used to power the device.

Figure 16 illustrates a comparison between a typical off-the-shelf power converter and the converter designed specifically for this application and their common mode currents induced while operating with changing load power. The off-the-shelf converter was loaded with 20x lower power but generated a few times higher common mode current.

7. Device performance

The rotational seismology needs sensors operating in the frequency range from 0.01 Hz up to 100 Hz, with a sensitivity up low as 10^{-8} rad/s. The optical rotational sensors based on a fiber optic gyroscope operating as devices



Fig. 16. Comparison of common mode noise between an off-the-shelf converter (violet plot) and IPC (blue plot).

with time dependent instrument use the Allan variance (AV) analysis for investigating their fundamental noise performance [24,25]. Figure 17 presents the results for this analysis for the tested FOS5, whereas Figure 18 presents the ASD noise in the seismometer required band. Contrary to previous plots, other factors have impact on these characteristics - such as Modulator module (fiber loop length optimization – curve I and II), control algorithm, external conditions (curve III with optimized temperature control – without IPC). The plots depicted concern FOS5 operating in stable laboratory conditions, in a limited noise environment, outside the urban area. The data have been collected in Warsaw, Poland during a period of 2 hours between 24:00 and 2:00 am. Two important parameters result from the AV plot. The first one is the angular random walk (ARW) which represents sensitivity at Hertz for 1 s of data acquisition time, whereas the second bias instability (BI) – minimum of the characteristics – represents the device drift. As visible in the plots, the best parameter values were obtained for curve III - system operating with optimized parameters and internal temperature reduced – and are equal to ARW – $3 \cdot 10^{-7}$ rad/s, BI – $3 \cdot 10^{-8}$ rad/s.

A self-noise analysis is presented in a form of the SD noise in Fig. 18 showing the best system performance for curve III. The presented self-noise is the output of the sensor operating at rest, when no input motion is applied. The calculated ASD characteristics were filtered using a Konno-Ohmachi filter [26] with smoothing coefficient equal to 40.

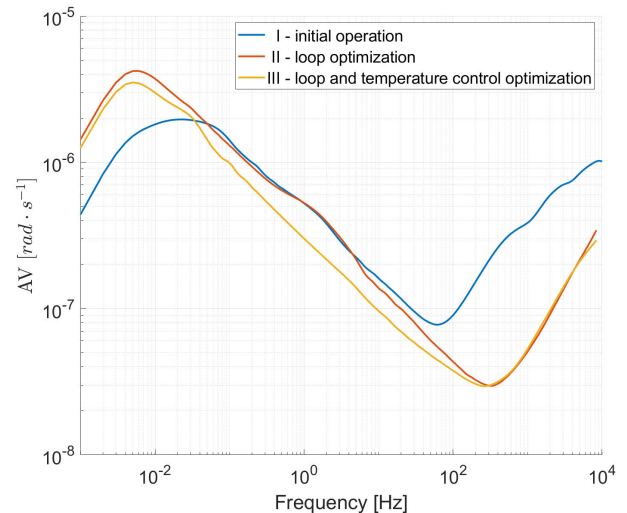


Fig. 17. Graph presenting FOS5 Allan variance analysis.

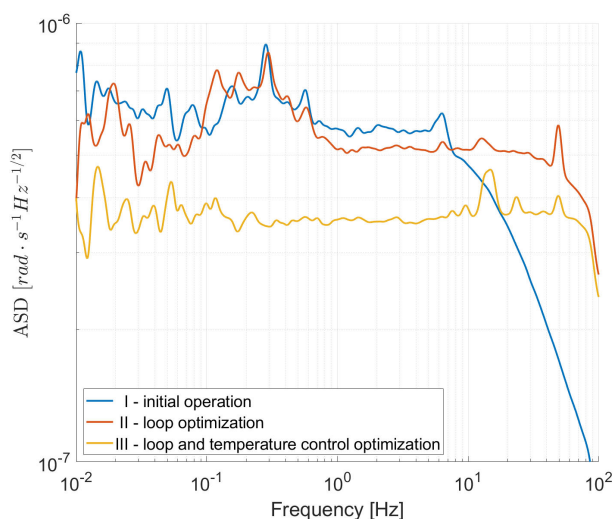


Fig. 18. FOS5 performance across its nominal operating band. ASD noise for optimizing different device parameters: Curves: I – device operation in a hermetic shelling, II – operation with the Modulator module optimised to sensor loop length, III – operation with IPC omitted (lower internal device temperature).

Comparison of Figs. 17 and 18 with previous plots (Fig. 15) shows that the APD diode noise level is the bottom limit for the entire device noise, but the device can operate as low as this limit, thus achieving ASD lower than $4 \cdot 10^{-7}$ rad/(s $\sqrt{\text{Hz}}$) in most of the operation frequency range. Low-frequency perturbations were eliminated and the ASD characteristics is mostly flat in the whole range.

8. Conclusions

The main aim of this research was to discover the magnitudes of the noise generated by various stages of the Sensor module, compare it with optical circuit noise and address the overall device precision. Electronic circuit can handle the precision of the optical components used, keeping a reasonable margin. Investigation on the performance of other available APDs may be conducted to see whether a better device performance can be obtained. The measurements additionally indicate significant factors affecting the noise levels in certain situations, such as the presence of the analog circuitry shield or the transimpedance amplifier analog filter. Preliminary research has been conducted on the influence of selecting the best powering scheme for the device. The IPC introduces little, negligible noise, while providing significantly better common mode insulation for any outside interferences than other power converters available. Although the IPC is recommended for use, its application in an isolated hermetic case should be subjected to more extensive temperature optimization tests, for all FOS5 operations as shown in the last section.

Authors' statement

S. Niespodziany: article preparation, as well as FOS5 electronic part construction and data processing; A. T. Kurzych: FOS5 optical part construction and investigation; M. Dudek: FOS5 Allan variance and ASD analysis conducting and graphs preparation.

Acknowledgements

This work was supported by the program POIR 04.02.00-14-A003/16 “EPOS – System Obserwacji Płyty Europejskiej”.

References

- [1] Rajan, G. *Optical Fiber Sensors: Advanced Techniques and Applications*. (CRC press, 2017).
- [2] Sabri, N., Aljunid, S. A., Salim, M. S., Ahmad, R. B. & Kamaruddin, R. Toward optical sensors: Review and applications. *J. Phys.: Conf. Ser.* **423**, 012064 (2014). <https://doi.org/10.1088/1742-6596/423/1/012064>
- [3] Lee, B. et al. Interferometric fiber optic sensors. *Sensors* **12**(3), 2467-2486 (2012). <https://doi.org/10.3390/s120302467>
- [4] Bao, X. & Chen, L. Recent progress in distributed fiber optic sensors. *Sensors* **12**(7), 8601-8639 (2012). <https://doi.org/10.3390/s120708601>
- [5] Liu, G., Han, M. & Hou, W. High-resolution and fast-response fiber-optic temperature sensor using silicon Fabry-Pérot cavity. *Opt. Express* **23**(6), 7237-7247 (2015). <https://doi.org/10.1364/OE.23.007237>
- [6] Campanella, C. E., Cuccovillo, A., Campanella, C., Yurt, A. & Passaro, V. Fibre Bragg grating based strain sensors: review of technology and applications. *Sensors* **18**(9), 3115 (2018). <https://doi.org/10.3390/s18093115>
- [7] Ramakrishnan, M., Rajan, G., Semenova, Y. & Farrell, G. Overview of fiber optic sensor technologies for strain/temperature sensing applications in composite materials. *Sensors* **16**(1), 99 (2016). <https://doi.org/10.3390/s16010099>.
- [8] Yu, Q. & Zhou, X. (2011) Pressure sensor based on the fiber-optic extrinsic Fabry-Perot interferometer. *Photonic Sens.* **1**(1), 72-83 (2011). <https://doi.org/10.1007/s13320-010-0017-9>
- [9] Chang, T. et al. Fiber optic interferometric seismometer with phase feedback control. *Opt. Express* **28**(5), 6102-6122 (2020). <https://doi.org/10.1364/OE.385703>
- [10] Budinski, V. & Donlagic, D. Fiber-optic sensors for measurements of torsion, twist and rotation: a review. *Sensors* **17**(3), 443 (2017). <https://doi.org/10.3390/s17030443>
- [11] Jaroszewicz, L. R., Kurzych, A., Krajewski, Z., Kowalski, J. K., Kowalski, H. A. & Teisseyre, K. P. Innovative Fibre-Optic Rotational Seismograph. in *7th International Symposium on Sensor Science Proceedings* **15**, 45 (2019). <https://doi.org/10.3390/proceedings2019015045>
- [12] Lee, W. H. K., Celebi, M., Todorovska, M. & Igel, H. Introduction to the special issue on rotational seismology and engineering applications. *Bull. Seismol. Soc. Am.* **99**, 945-957 (2009). <https://doi.org/10.1785/0120080344>
- [13] Kurzych, A., Kowalski, J. K., Sakowicz, B., Krajewski, Z. & Jaroszewicz, L. R. The laboratory investigation of the innovative sensor for torsional effects in engineering structures' monitoring. *Opto-Electron. Rev.* **24**(3), 134-143 (2016). <http://dx.doi.org/10.1515/oere-2016-0017>
- [14] Kurzych, A., Jaroszewicz, L. R., Kowalski, J. K. & Sakowicz, B. Investigation of rotational motion in a reinforced concrete frame construction by a fiber optic gyroscope. *Opto-Electron. Rev.* **28**(2), 69-73 (2020). <https://doi.org/10.24425/opelre.2020.132503>
- [15] Bernauer, F. et al. Rotation, strain, and translation sensors performance tests with active seismic sources. *Sensors* **21**(1), 264 (2021). <https://doi.org/10.3390/s21010264>
- [16] Sagnac, G. The light ether demonstrated by the effect of the relativewind in ether into a uniform rotation interferometer. *Acad. Sci.* **95**, 708-710 (1913).
- [17] Post, E. J. Sagnac effect. *Rev. Mod. Phys.* **39**, 475-493 (1967). <https://doi.org/10.1103/RevModPhys.39.475>
- [18] Jaroszewicz, L. R., Kurzych, A., Krajewski, Z., Dudek, M., Kowalski, J. K. & Teisseyre, K. P. The fiber-optic rotational seismograph - laboratory tests and field application. *Sensors* **19**(12), 2699 (2019). <https://doi.org/10.3390/s19122699>
- [19] Lefevre, H. C., Martin, P., Morisse, J., Simonpietri, P., Vivenot, P. & Arditti, H. J. High-dynamic-range fiber gyro with all-digital signal processing. *Proc. SPIE* **1367**, 72-80 (1991).

- [20] LeFevre, H. C. *The Fiber Optic Gyroscope*. (2nd ed.) 154–196 (Artech House: Norwood, MA, 2008).
- [21] Merlo, S., Norgia, M. & Donati, S. Fiber Gyroscope Principles. in *Handbook of Fibre Optic Sensing Technology*. (ed. Lopez, J. M.) 1–23 (2000).
- [22] Bernauer, F., Wassermann, J. & Igel, H. Rotational sensors—A comparison of different sensor types. *J. Seismol.* **16**, 595–602 (2012). <https://doi.org/10.1007/s10950-012-9286-7>
- [23] Heinzl, G., Rüdiger, A. & Schilling, R. Spectrum and spectral density estimation by the Discrete Fourier transform (DFT), including a comprehensive list of window functions and some new at-top windows. https://holometer.fnal.gov/GH_FFT.pdf (2021).
- [24] IEEE Standard Specification Format Guide and Test Procedure for Single-Axis Interferometric Fiber Optic Gyros. *IEEE-SA Standards Board* **952**, (1997). <https://doi.org/10.1109/IEEESTD.1998.86153>
- [25] Allan Variance: Noise Analysis for Gyroscopes. Application Note AN5087 Rev. 0.2/2015. Freescale Semiconductor Inc., Eindhoven, Netherlands, (2015).
- [26] Konno K. & Ohmachi, T. Ground motion characteristics estimated from spectral ratio between horizontal and vertical components of microtremor. *Bull. Seismol. Soc. Am.* **88**(1), 228-241 (1998).